Inorganic Chemistry
Article
pubs.acs.org/IC

Hydrothermal Synthesis and Dehydration of $CaTeO_3(H_2O)$: An Original Route to Generate New $CaTeO_3$ Polymorphs

Morgane Poupon,[†] Nicolas Barrier,*[,†] Sebastien Petit,[†] Simon Clevers,[‡] and Valerie Dupray[‡]

[†]Laboratoire CRISMAT, UMR 6508 CNRS ENSICAEN, 6 bd Maréchal Juin, 14050 CAEN Cedex 4, France
[‡]Crystal Genesis Unit, SMS EA 3233, Normandie Université, Université de Rouen, F-76821 Mont-Saint-Aignan Cedex, France

Supporting Information

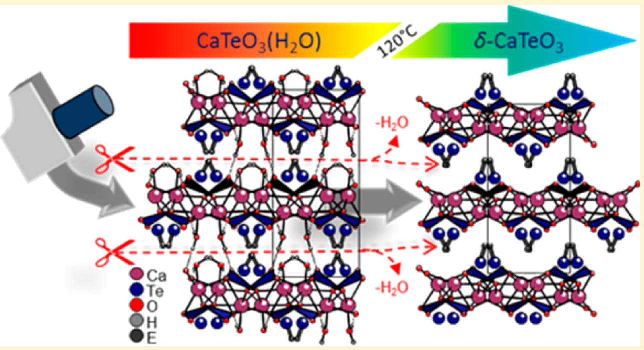

ABSTRACT: $CaTeO_3(H_2O)$ was obtained from microwave-assisted hydrothermal synthesis as a polycrystalline sample material. The dehydration reaction was followed by thermal analysis (thermogravimetric/differential scanning calorimetry) and temperature-dependent powder X-ray diffraction and leads to a new δ-$CaTeO_3$ polymorph. The crystal structures of $CaTeO_3(H_2O)$ and δ-$CaTeO_3$ were solved ab initio from PXRD data. $CaTeO_3(H_2O)$ is non-centrosymmetric: $P2_1cn$; $Z = 8$; $a = 14.785\,49(4)$ Å; $b = 6.791\,94(3)$ Å; $c = 8.062\,62(3)$ Å. This layered structure is related to the ones of $MTeO_3(H_2O)$ (M = Sr, Ba) with layers built of edge-sharing $[CaO_6(H_2O)]$ polyhedra and are capped of each side by $[Te^{IV}O_3E]$ units. Adjacent layers are stacked along the *a*-axis and are held together by H-bonds via the water molecules. The dehydration reaction starts above 120 °C. The transformation of $CaTeO_3(H_2O)$ into δ-$CaTeO_3$ ($P2_1ca$; $Z = 8$; $a = 13.3647(6)$ Å; $b = 6.5330(3)$ Å; $c = 8.1896(3)$ Å) results from topotactic process with layer condensation along the *a*-axis and the $1/2b$ translation of intermediate layers. Thus, δ-$CaTeO_3$ stays non-centrosymmetric. The characteristic layers of $CaTeO_3(H_2O)$ are also maintained in δ-$CaTeO_3$ but held together via van der Waals bonds instead of H-bonds through water molecules. Electron localization function and dipole moment calculations were also performed. For both structures and over each unit cell, the dipole moments are aligned antiparallel with net dipole moments of 3.94 and 0.47 D for $CaTeO_3(H_2O)$ and δ-$CaTeO_3$, respectively. The temperature-resolved second harmonic generation (TR-SHG) measurements, between 30 and 400 °C, show the decreasing of the SHG intensity response from 0.39 to 0.06 × quartz for $CaTeO_3(H_2O)$ and δ-$CaTeO_3$, respectively.

1. INTRODUCTION

The synthesis and the characterization of new materials with non-centrosymmetric crystal structure arouse interest of many laboratories in the field of solid-state chemistry. Indeed the non-centrosymmetry is the first condition needed for a material to present functional properties such as piezoelectricity, pyroelectricity, ferroelectricity, or second harmonic generation for nonlinear optical properties.[1] For the pyroelectric and ferroelectric properties there is one more condition: the material must be polar with a nonzero macroscopic dipole moment. When a chemist needs to synthesize such materials he must consider what could favor non-centrosymmetry as well as the polarity. One answer consists in using cations subject to second-order Jahn–Teller (SOJT) distortions able to provide asymmetric coordination environments with local dipole moments.[2] For example it is known that for oxides, d^0 cations such as Ti^{IV}, Nb^V, Mo^{VI}, W^{VI}, etc. exhibit SOJT distortions for their octahedral environment. Another interesting family of cations that present SOJT distortions are the ones with active nonbonded electron pair such as Pb^{II}, Sn^{II}, Sb^{III}, Bi^{III}, Se^{IV}, Te^{IV}, and I^V. Among those cations, Te^{IV} is rather of interest due to the numbers of providing coordination environments: $[TeO_3E]$, $[TeO_4E]$, and $[TeO_5E]$, where E denotes the nonbonded electron pair.

Many tellurium(IV) oxides have non-centrosymmetric structures and thus were studied for their interesting physical properties. This is the case of $MTeO_3$ oxides with M = Ca, Sr, Ba, Zn, Cd, Hg, Pb, Ni, which show nonlinear optical properties,[3,4] and of oxides such as $CaTeO_3$ and $SrTeO_3$, which are ferroelectrics.[5,6] Moreover, the two latter compounds exhibit numerous polymorphs, whose structures have just recently been solved. For $CaTeO_3$[7] and $SrTeO_3$[8] three and four polymorphs have been reported, respectively. All these polymorphic phases were obtained using classical solid-state synthesis with TeO_2 and MCO_3 or MO (M = Ca, Sr) as starting reagents, with heating temperatures ranging between 700 and 900 °C. Another preparation route was reported for α-$CaTeO_3$ and α-$SrTeO_3$, using "chimie douce" reaction route via the synthesis of hydrated oxotellurate(IV) $MTeO_3(H_2O)$ followed by dehydration reaction.[9] Nevertheless, no original structure of $MTeO_3(H_2O)$ has been reported, and no new

Received: January 8, 2015
Published: June 2, 2015

$MTeO_3$ (M = Ca, Sr) polymorph has been mentioned. But recently, we have shown that the hydrothermal synthesis of $SrTeO_3(H_2O)$ followed by the dehydration versus temperature allows the generation of a new ε-$SrTeO_3$ polymorph.[10]

Following precedent example of $SrTeO_3(H_2O)$, we present hereafter the hydrothermal synthesis of $CaTeO_3(H_2O)$ and the description of its original and non-centrosymmetric structure, as well as the complete study of the dehydration process versus temperature leading to the new δ-$CaTeO_3$ polymorph also non-centrosymmetric. We also report the infrared spectrum of $CaTeO_3(H_2O)$ and the nonlinear optical properties of $CaTeO_3(H_2O)$ and δ-$CaTeO_3$, which were studied from temperature-resolved second harmonic generation measurements, as well as the thermal behavior of $CaTeO_3(H_2O)$ and δ-$CaTeO_3$.

2. EXPERIMENTAL SECTION

2.1. Synthesis. The hydrated compound $CaTeO_3(H_2O)$ can be obtained by microwave-assisted hydrothermal synthesis. The synthesis was performed with a Mars5 CEM microwave furnace. In a Teflon-lined autoclave (XP1500 by CEM), 1 equiv of $Ca(NO_3)_2$ (6.28 mmol), 1 equiv of TeO_2 (6.28 mmol), and 3 equiv of NaOH (18.84 mmol) were introduced with 30 mL of distilled water. The autoclave was placed in a microwave furnace at a power of 1600 W. The temperature was ramped over 20 min to 185 °C and then held for 1 h before being decreased to room temperature by furnace inertia. The final product was filtered, washed with distilled water and ethanol, and then was dried in a desiccator overnight. We obtained a monophasic microcrystalline powder but without crystal of sufficient size to perform single-crystal X-ray diffraction measurements. Energy-dispersive X-ray spectroscopy analyses performed on these crystallites give a cationic ratio Ca/Te close to 1. (Table S1 of the Supporting Information)

We also tried to grow single crystal from "classic" hydrothermal synthesis. The same mixture was introduced in a 50 mL polytetrafluoroethylene insert with 10 mL of deionized water. The insert was transferred in a Berghof stainless steel pressure digestion vessel then heated from room temperature to 185 °C in 5 h 20 min, left at 185 °C during 72 h, and cooled to room temperature in 10 h. We also obtained a polycrystalline sample of $CaTeO_3(H_2O)$ with an unidentified extra phase but without crystals of sufficient size to perform single-crystal X-ray diffraction measurements.

Finally, all studies presented hereafter were performed on monophasic polycrystalline samples obtained from microwave-assisted hydrothermal synthesis.

2.2. Powder X-ray Diffraction. The powder X-ray diffraction (PXRD) data were recorded on a Bruker D8 advance diffractometer equipped with a primary germanium (111) Johansson monochromator ($\lambda K_{\alpha 1}$ = 1.5406 Å) and a Lynxeye detector. For $CaTeO_3(H_2O)$ the diffractogram was collected, at room temperature in the 2θ range of 5−140° with a step size of ~0.009° and a time per step of 4.8 s. Temperature-dependent powder X-ray diffraction (TD-PXRD) data were recorded on the same diffractometer with an Anton Paar HTK1200N chamber, under N_2 flux, every 30 °C until 960 °C. For the structural study of δ-$CaTeO_3$ the X-ray diffraction pattern was collected in air at 400 °C in the 2θ range of 10−130° with a step size of ~0.012° and a time per step of 1 s.

2.3. Structure Determinations. The crystal structures of $CaTeO_3(H_2O)$ and δ-$CaTeO_3$ were solved ab initio from PXRD data. All refinement parameters for the two structures are listed in Table 1. Table 2 indicates atomic positions and isotropic displacement parameters (U_{iso}), and Table 3 presents a selection of interatomic distances for the two phases. The bond valence sums (BVS)[11] were calculated for both structures with parameters provided by Brese and O'Keeffe[12] and are shown in Table 4. Additional crystallographic information is available in the Supporting Information.

The $CaTeO_3(H_2O)$ PXRD pattern (Figure 1) was indexed with the DICVOL06 software[13] in an orthorhombic unit cell with parameters a = 14.779 Å, b = 6.789 Å, c = 8.059 Å and following figures of merit: $M(20)$ = 309.4, $F(20)$ = 513.8 (0.0011, 37). A second harmonic generation (SHG) qualitative test was performed on a white powder sample of $CaTeO_3(H_2O)$, in transmission configuration. A notable SHG signal was observed, which proved that the crystal structure of this compound is non-centrosymmetric. Thus, the structure was solved with the EXPO2004 software[14] in the non-centrosymmetric space group $P2_1cn$. The Rietveld refinements were performed with the JANA2006 software[15] taking into account U_{iso} parameters. The preferred orientation phenomena observed on the diffraction pattern, due to the orientation of the crystallites along the a-axis, was corrected with the March and Dollase model.[16] Both refined parameters of preferred orientation along the a-axis are smaller than one with respective values of 0.57 and 0.59, which is consistent with crystallites in platelike shape. For the last refinements, to get U_{iso} parameters with the meaningful standard deviations, a single atomic displacement parameter was refined for all oxygen atoms. The reliability factors obtained are R_{Fobs} = 3.66% and R_{wp} = 9.61%.

The δ-$CaTeO_3$ phase is metastable and is the first polymorphic form obtained after the dehydration of $CaTeO_3(H_2O)$. Despite anisotropic peak broadening the PXRD pattern recorded at 400 °C (Figure 2) could be indexed with the DICVOL06 program in an orthorhombic unit cell with parameters a = 13.3647 Å, b = 6.5330 Å, c = 8.1896 Å, and the following figures of merit: $M(20)$ = 17.1, $F(20)$ = 27.5 (0.0152, 48). Examination of the indexed pattern within the $Pmmm$ space group shows the following reflection conditions ($h0l$) with $l = 2n$ and ($hk0$) with $k = 2n$. Those reflection conditions are consistent with the $Pmca$ and $P2_1ca$ space groups. SHG measurements were performed at 400 °C on this δ-$CaTeO_3$ phase. A SHG response is observed on the corresponding spectrum but with a weak intensity. Thus, we may wonder if this structure is non-centrosymmetric or not. After few unsuccessful attempts using the centrosymmetric space

Table 1. Details of PXRD Data and Rietveld Refinements for $CaTeO_3(H_2O)$ and δ-$CaTeO_3$

diffractometer	Bruker D8 advance vario1	
radiation (Å)	Cu $K\alpha_1$ radiation λ = 1.5406	
compound	$CaTeO_3(H_2O)$	δ-$CaTeO_3$
2θ-range/step (deg)/time per step (s)	5−139.991/~0.009/4.8	10−126.181/~0.012/1
temperature (°C)	20	400
space group	$P2_1cn$	$P2_1ca$
Z	8	8
a /Å	14.78549(4)	13.3647(7)
b /Å	6.79194(3)	6.5330(3)
c /Å	8.06261(3)	8.1896(3)
V /Å^3	809.665(6)	715.05(8)
molar mass (g mol^{-1})	233.7	215.7
Rietveld refinement:		
shape	pseudo-Voigt	pseudo-Voigt
background	15 Legendre polynoms	11 Legendre polynoms
preferred orientation	March and Dollase ; a-axis	March and Dollase; a-axis
asymmetry	Finger, Cox, and Jephcoat	Finger, Cox, and Jephcoat
anisotropic reflection broadening	Stephens	Stephens
Rietveld agreement indices		
R_{Fobs}	0.0366	0.0405
R_{Bobs}	0.0643	0.0543
Rwp	0.0961	0.0989
$cRwp$	0.1578	0.1663
GOF	1.70	1.13

Table 2. Atomic Positions and U_{iso} Parameters for $CaTeO_3(H_2O)$ for δ-$CaTeO_3$

$CaTeO_3(H_2O)$					
atom	Wyckoff	*x*	*y*	*z*	U_{iso} (Å^2)
Ca1	4*a*	0.0644(2)	0.6313(8)	0.9531(6)	0.0073(11)
Ca2	4*a*	0.1540(3)	0.1291(7)	0.8304(6)	0.0057(10)
Te1	4*a*	0.24723(9)	0.6555(3)	0.71323(16)	0.0057(4)
Te2	4*a*	0.4628	0.6594(3)	0.43016(17)	0.0038(3)
O1	4*a*	0.1969(7)	0.464(2)	0.8546(18)	0.0068(12)
O2	4*a*	0.1476(9)	0.815(2)	0.7087(15)	0.0068(12)
O3	4*a*	0.2324(8)	0.5436(19)	0.4993(19)	0.0068(12)
O4	4*a*	0.5090(7)	0.4525(19)	0.559(2)	0.0068(12)
O5	4*a*	0.5730(9)	0.810(2)	0.4275(17)	0.0068(12)
O6	4*a*	0.4694(7)	0.5131(18)	0.2186(16)	0.0068(12)
Ow1 (water molecule 1)	4*a*	0.2870(8)	0.112(2)	0.6490(18)	0.0068(12)
Ow2 (water molecule 2)	4*a*	0.4342(8)	0.108(2)	0.3615(17)	0.0068(12)
δ-$CaTeO_3$					
atom	Wyckoff	*x*	*y*	*z*	U_{iso} (Å^2)
Ca1	4*a*	0.0646(8)	0.5998(18)	0.9196(11)	0.037(4)
Ca2	4*a*	0.1373(7)	0.1031(16)	0.8060(11)	0.026(4)
Te1	4*a*	0.2666(3)	0.5875(6)	0.6663(3)	0.0319(19)
Te2	4*a*	0.4362	0.0843(7)	0.4467(3)	0.041(2)
O1	4*a*	0.2069(18)	0.801(4)	0.811(3)	0.035(4)
O2	4*a*	0.150(3)	0.439(5)	0.678(3)	0.035(4)
O3	4*a*	0.242(2)	0.718(4)	0.472(3)	0.035(4)
O4	4*a*	0.5016(19)	0.269(4)	0.586(3)	0.035(4)
O5	4*a*	0.562(3)	0.907(6)	0.464(3)	0.035(4)
O6	4*a*	0.4732(17)	0.178(3)	0.218(3)	0.035(4)

group *Pmca* the structure was finally solved in the non-centrosymmetric space group $P2_1ca$ with the EXPO2004 program. The Rietveld refinements were performed with the JANA2006 program from the atomic positions previously obtained with EXPO2004 program taking into account U_{iso} parameters. The preferred orientation of the crystallites along the *a*-axis was corrected using the model of March and Dollase. The phenomenological model developed by Stephens[17] was used during the refinement to take into account the XRD anisotropic peak broadening. On the PXRD diagram at high angle (Figure 2), the reflections are not very well-resolved with low intensities. This does not enable to refine independent U_{iso} parameters for each light atom. Thus, to get all U_{iso} parameters with the meaningful standard deviations, a single U_{iso} was refined for all oxygen atoms. The final agreement factors obtained at the end of the last series of refinements are relatively low: R_{Fobs} = 4.05%, R_{wp} = 9.87%. The absence of additional symmetry and especially of an inversion center was checked with the ADSYM tool available in the PLATON program.[18]

2.4. Thermal Analysis. Thermogravimetric (TG) and differential scanning calorimetry (DSC) measurements were performed simultaneously on microcrystalline powder sample of $CaTeO_3(H_2O)$ on a Netzsch STA 449F3 system. The sample was placed in a platinum pan and heated at a rate of 10 °C·min^{-1} in a flowing nitrogen atmosphere (20 mL·min^{-1}) between 30 and 1000 °C.

2.5. Vibrational Spectroscopy. The infrared spectra of a polycrystalline sample of $CaTeO_3(H_2O)$, were recorded in the spectral range between 4000 and 400 cm^{-1} with a PerkinElmer Spectrum100 instrument, with the powdered sample dispersed in KBr.

2.6. Electronic Structure Calculation. The electronic structures of $CaTeO_3(H_2O)$ and δ-$CaTeO_3$ were calculated through the density functional theory (DFT). We used the CRYSTAL14 software[19] with B3LYP approximation, Stuttgart core pseudopotentials (ECP28MDF), and a valence double-ζ basis for tellurium atoms,[20] the Hay-Wadt small-core ECP with 31(1d)G basis set for calcium atoms,[21] a 8−411(1d)G basis set for oxygen atoms,[22] and a 3−1(p)G basis set for hydrogen atoms.[23] For the hydrated phase, the unknown positions of the hydrogen atoms were found by using a geometry optimization keeping constant the unit-cell parameters and the positions of the others atoms. To accurately localize the 5s^2 electron lone pairs E associated with the tellurium atoms, an analysis of the electron localization function (ELF) was performed. Grid files of the electronic density and of the ELF were first obtained by the TOPOND14 code.[23] Then we used critic2 software[24] to seek the critical point of the ELF and to calculate the electronic charge inside basins.

To find the direction and the magnitude of the local dipole moments associated with the $[Te^{IV}O_3E]$ polyhedra for both $CaTeO_3(H_2O)$ and δ-$CaTeO_3$ structures, we first evaluated the dipole moment of each Te−O bond using partial charge of oxygen atoms extracted from a Mulliken population analysis of the DFT calculation, as well as the position and the electronic charge of the lone pair E. Then a vector sum of the dipole moments for the lone pair and the three Te−O bonds gives a net local dipole moment.

The results of the electronic structure calculations of $CaTeO_3(H_2O)$ and δ-$CaTeO_3$, that is, the localizations of the hydrogen atoms and the electron lone pairs and the dipole moment calculations, are presented in Tables 5 and 6.

2.7. Second Harmonic Generation analysis. Temperature-resolved second harmonic generation (TR-SHG) measurements were recorded with the following equipment. A Nd:YAG Q-switched laser (Quantel) operating at 1.06 μm was used to deliver up to 360 mJ pulses of 5 ns duration with a repetition rate of 10 Hz. An energy adjustment device made of two polarizers (P) and a half-wave plate (λ/2) allowed the incident energy to vary from 0 to ca. 300 mJ per pulse. An RG1000 filter was used after the energy adjustment device to remove light from laser flash lamps. The samples (a few milligrams of powder in a crucible) were placed in a computer-controlled Heating−Cooling stage (Linkam THMS-600) and were irradiated with the laser beam (4 mm in diameter).

The signal generated by the sample (diffused light) was collected into an optical fiber (500 μm of core diameter) and directed onto the entrance slit of a spectrometer (Ocean Optics). A boxcar integrator allowed an average spectrum (spectral range of 490−590 nm) with a resolution of 0.1 nm to be recorded over 3 s (30 pulses). The incident energy was set at 70 mJ. For temperature-resolved measurements, the

Table 3. Selected Interatomic Distances for $CaTeO_3(H_2O)$ and δ-$CaTeO_3$

atom 1	atom 2	distance (Å)	atom 1	atom 2	distance (Å)
$CaTeO_3(H_2O)$					
Ca1	O1	2.407(12)	Ca2	O1	2.367(14)
	O2	2.636(14)		O2	2.357(15)
	O2	2.429(13)		O3	2.141(15)
	O4	2.338(14)		O4	2.610(12)
	O5	2.383(17)		O5	2.428(15)
	O6	2.211(14)		O5	2.596(15)
	Ow2	2.438(13)		Ow1	2.461(13)
Te1	O1	1.882(13)	Te2	O4	1.877(14)
	O2	1.821(14)		O5	1.938(14)
	O3	1.894(16)		O6	1.978(14)
O1	O2	2.75(2)	O2	O3	2.80(2)
	O3	2.95(2)		O3	2.84(2)
	O5	2.738(19)		O4	2.932(18)
	Ow1	2.776(19)		O5	2.98(2)
O4	O5	2.82(2)		Ow1	2.932(19)
	O6	2.85(2)	O5	Ow2	2.930(19)
	Ow2	2.70(2)	O6	Ow1	2.856(18)
δ-$CaTeO_3$					
atom 1	atom 2	distance (Å)	atom 1	atom 2	distance (Å)
Ca1	O1	2.48(3)	Ca2	O1	2.18(3)
	O2	2.52(3)		O2	2.44(3)
	O2	2.42(3)		O3	2.28(3)
	O4	2.32(3)		O4	2.29(3)
	O5	2.23(4)		O5	2.43(3)
	O6	2.20(3)		O5	2.49(3)
				O6	2.87(2)
Te1	O1	1.99(2)	Te2	O4	1.88(3)
	O2	1.84(4)		O5	2.04(4)
	O3	1.84(2)		O6	2.04(3)
				O6	2.85(3)
O1	O2	2.71(4)	O2	O3	2.89(4)
	O3	2.87(3)		O4	2.99(4)
	O5	2.77(4)		O5	2.80(5)
O4	O5	2.69(4)	O5	O6	2.93(4)
				O6	2.46(4)

Table 4. Individual Bond Valence Sums for $CaTeO_3(H_2O)$ and δ-$CaTeO_3$

$CaTeO_3(H_2O)$	BVS[a] (v.u.)	δ-$CaTeO_3$	BVS[a] (v.u.)
Ca1	2.26	Ca1	2.23
Ca2	2.23	Ca2	2.30
Te1	4.02	Te1	3.95
Te2	3.47	Te2	3.13
O1	1.94	O1	1.79
O2	2.30	O2	2.26
O3	1.87	O3	1.97
O4	1.87	O4	2.11
O5	1.94	O5	1.87
O6	1.53	O6	1.60
Ow1 (water molecule 1)	0.27/1.78[b]		
Ow2 (water molecule 2)	0.28/1.82[b]		

[a] Bond valence parameters: Te–O: R_0 = 1.977 Å; B = 0.37 Å ; H–O: R_0 = 0.907 Å ; B = 0.28 Å, for d(H–O) < 1.05 Å ; Ca–O: R_0 = 1.967 Å; B = 0.37 Å. Bond valence = $\exp((R_0 - R)/B)$. [b] BVS with H atoms from geometry optimization (see Table 5).

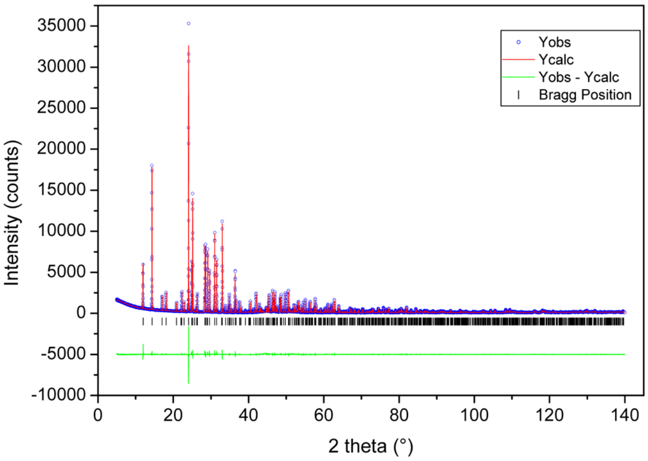

Figure 1. PXRD diagram of $CaTeO_3(H_2O)$ (Cu Kα1 radiation; 1.5406 Å) with observed (○), calculated (red), Bragg reflections (vertical tick marks), and difference profiles (green), obtained after Rietveld refinements.

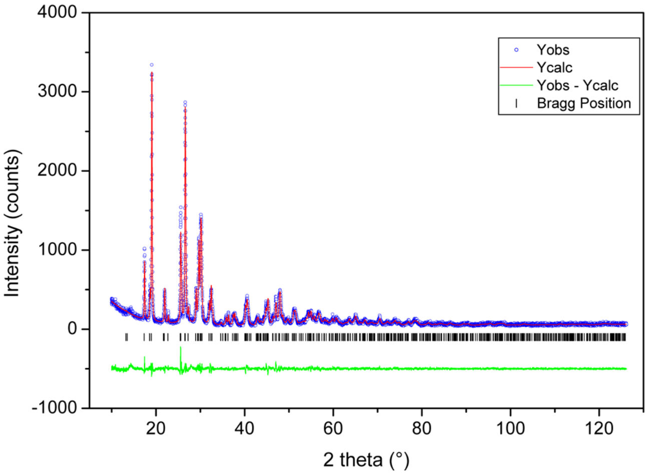

Figure 2. PXRD diagram of δ-$CaTeO_3$ recorded at 400 °C in air, with observed (○), calculated (red), Bragg reflections (vertical tick marks) and difference profiles (green), obtained after Rietveld refinements.

SHG response was recorded between 20 and 500 °C with a heating rate of 5 °C·min^{-1}.

According to the Kurtz and Perry SHG powder method,[25] SHG signal intensities were compared to the signal of a reference compound (α-quartz powder 45 μm average size).

3. RESULTS AND DISCUSSION

3.1. Crystal Structures and Dehydration Reaction. The structure of the hydrated compound $CaTeO_3(H_2O)$ (Figure 3) is related to those of $SrTeO_3(H_2O)$[10] and $BaTeO_3(H_2O)$.[26] Indeed, these three structures can be described from the stacking of layers that are built of $[AO_6(H_2O)]$ polyhedra (A = Ca, Sr, Ba) and isolated $[Te^{IV}O_3E]$ units. In these three structures, the $[AO_6(H_2O)]$ polyhedra present the same distortion, intermediate between a monocapped octahedron and a pentagonal bipyramid. In $CaTeO_3(H_2O)$ the Ca–O distances range between 2.21(1) and 2.64(2) Å for the Ca1 atom and between 2.14(2) and 2.61(1) Å for the Ca2 atom. The average distances of 2.41 and 2.42 Å related to the Ca1 and Ca2 atoms, respectively, are in good agreement with the sum of the ionic radii rCa^{2+} and rO^{2-} of 2.40 Å.[27] As in most oxotellurate compounds, the electronic lone pair is stereoactive

Table 5. Results of the Electronic Structure Calculation of $CaTeO_3(H_2O)$: Electron Lone Pairs and Hydrogen Atoms Positions, Hydrogen Bonds, and Dipole Moment Calculations

electron lone pairs						
	position					
electronic lone pair	*x*	*y*	*z*	Te−E/d(Å)	charge (e^-)	*V* ($Å^3$)
E1	0.335 67	0.720 20	0.732 68	Te1−E1/1.39	−2.62	14.68
E2	0.385 36	0.759 37	0.474 70	Te2−E2/1.38	−2.71	15.07

hydrogen atoms and hydrogen bonds									
atom	*x*	*y*	*z*	D	A	d_{D-H} (Å)	d_{A-H} (Å)	d_{D-A} (Å)	∠(DHA) (deg)
H1a	0.85061	0.93433	0.34231	Ow1	O6	0.98	1.89	2.86	168.8
H1b	0.76555	0.91335	0.46373	Ow1	O1	0.99	1.81	2.78	165.5
H2a	0.39915	0.27297	0.85495	Ow2		0.97			
H2b	0.45810	0.41310	0.74692	Ow2	O4	1.00	1.71	2.70	174. 1

dipole moments				
	vector (D)			
unit	*x*	*y*	*z*	magnitude (D)
(Te1)O_3E	−11.67	−0.46	−1.46	11.77
(Te2)O_3E	10.69	−2.73	−0.68	11.05
Unit-cell	−3.94	0	0	3.94

Table 6. Results of the Electronic Structure Calculation of δ-$CaTeO_3$: Electron Lone Pairs and Hydrogen Atoms Positions, Hydrogen Bonds, and Dipole Moment Calculations

electron lone pairs						
	position					
electronic lone pair	*x*	*y*	*z*	Te−E/d(Å)	charge (e^-)	*V* ($Å^3$)
E1	0.35671	0.47846	0.71418	Te1−E1/1.46	−2.72	19.07
E2	0.33995	0.04459	0.50643	Te2−E2/1.40	−2.81	19.18

dipole moments				
	vector (D)			
unit	*x*	*y*	*z*	magnitude (D)
(Te1)O_3E	−9.64	4.97	−4.93	11.91
(Te2)O_3E	9.76	0.39	−5.44	11.18
Unit-cell	−0.47	0	0	0.47

and thus acts as an anion in the local Te^{IV} coordination sphere. The [$Te^{IV}O_3E$] triangular-based pyramids are quite distorted in $CaTeO_3(H_2O)$, while they are much more regular in $SrTeO_3(H_2O)$ and $BaTeO_3(H_2O)$. The average distances in the calcium compound are d(Te1−O) = 1.87 Å and d(Te2−O) = 1.93 Å, with large standard deviations of 0.04 and 0.05 Å, respectively. For $SrTeO_3(H_2O)$ the average distance is d(Te−O) = 1.865 Å with a standard deviation of 0.006 Å, and for $BaTeO_3(H_2O)$ the average distance is d(Te−O) = 1.860 Å with a standard deviation of 0.004 Å. The electron lone pairs of the tellurium atoms are located between the layers, as observed in $SrTeO_3(H_2O)$. The Te−E distances of both tellurium atoms are quite similar to 1.39 Å for Te1−E1 and 1.38 Å for the Te2−E2. The calculated electronic charge associated with the E1 lone pair is equal to 2.62 e^- within a volume of 14.68 $Å^3$ and 2.71 e^- within a volume of 15.07 $Å^3$ for E2. Individual bond valence sums (BVS) were calculated and are shown in Table 4. For the calcium and Te1 atoms, individual BVS are close to the expected values: 2 (v.u.) and 4 (v.u.), respectively. For the Te2 and O6 atoms the BVS values, 3.47 (v.u.) and 1.51 (v.u.), respectively, are slightly lower than those expected. Just like other $ATeO_3(H_2O)$ (A = Sr, Ba) crystal structures, $CaTeO_3(H_2O)$ is built of edge-sharing [$CaO_6(H_2O)$] polyhedra in the (*bc*) plane, forming infinite layers (Figure 4a). Then, isolated [$Te^{IV}O_3E$] polyhedra are attached on each side of these layers. Along the *a*-axis these layers are held together through O−H···O hydrogen-bonding interactions. In $SrTeO_3(H_2O)$ each water molecule is involved in H-bonds between two successive layers providing in this way the cohesion of the crystal structure. In $CaTeO_3(H_2O)$, only the water molecule related to the Ow1 atom forms such interlayer H-bond, with a distance between hydrogen and acceptor of 1.89 Å for H1a···O6. The other H-bond H1b···O1 is an intralayer one of 1.81 Å. The water molecule formed with the Ow2 atom is not involved in interlayer H-bonds. Only one intralayer H-bond is created with hydrogen-acceptor distance of 1.71 Å for H2b···O4. For these oxygen atoms Ow1 and Ow2 related to the water molecules, individual BVS were calculated taking into account the four hydrogen atoms, localized by DFT and geometry optimization calculations. The BVS values are close to 2 (v.u.; see Table 4). Since $CaTeO_3(H_2O)$ crystallizes in the non-centrosymmetric polar 2*mm* point group, its structure should present a permanent dipole moment. Local dipole moments were calculated for the [$Te1O_3E$] and [$Te2O_3E$] polyhedra, and all the dipole moments were summed over the crystallographic unit-cell. As shown in Table 5, the magnitudes of the local dipole moments are quite similar for both polyhedra with 11.77 and 11.05 D, for

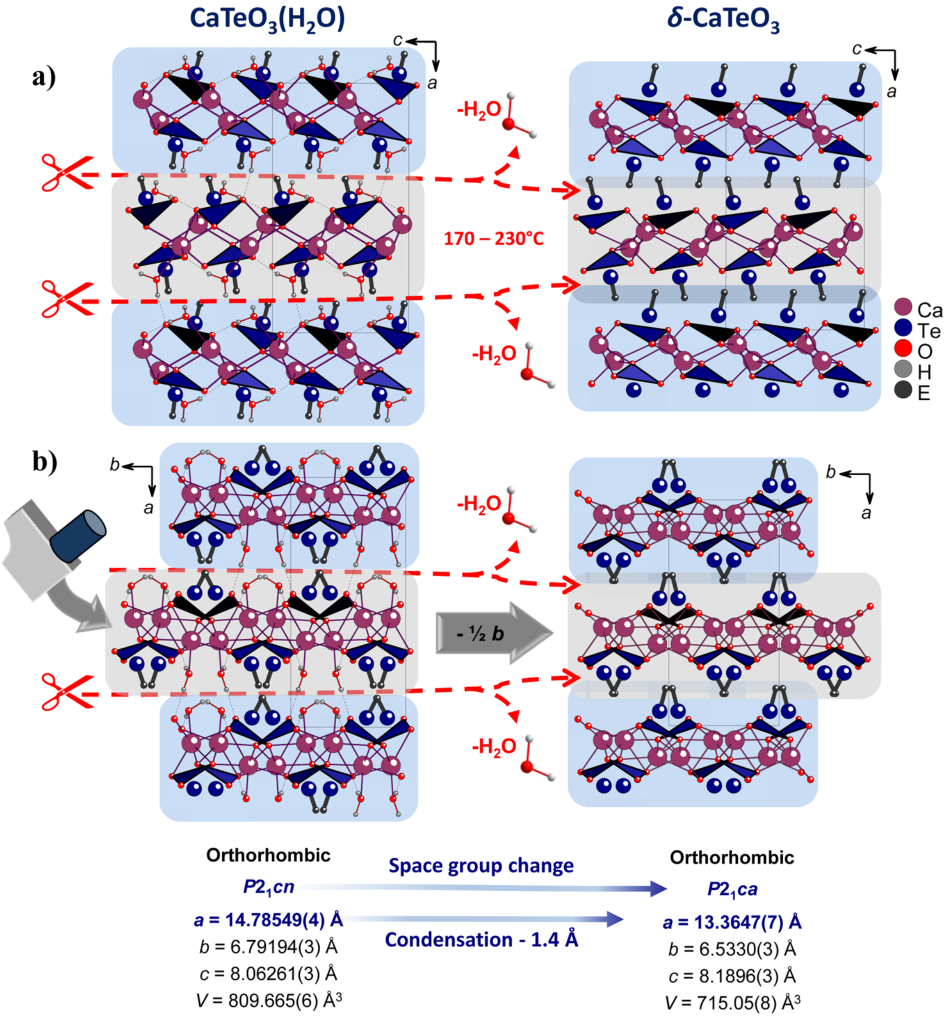

Figure 3. Dehydration process of $CaTeO_3(H_2O)$ into δ-$CaTeO_3$: views of $CaTeO_3(H_2O)$ and δ-$CaTeO_3$ structures (a) along the *b*-axis and (b) along the *c*-axis.

[$Te1O_3E$] and [$Te2O_3E$], respectively. In the structure (Figure 5a) the local dipole moments of both polyhedra are almost aligned antiparallel. The magnitude of net dipole moment over the unit cell is 3.94 D along the opposite direction to the *a*-axis. Such antiparallel alignments of the dipole moments as well as the low magnitude of the net dipole moment might prefigure a weak SHG response for $CaTeO_3(H_2O)$.

3.1.2. δ-$CaTeO_3$ and Dehydration Reaction. δ-$CaTeO_3$ is directly obtained from the dehydration of $CaTeO_3(H_2O)$ above 120 °C. On the PXRD diagram of δ-$CaTeO_3$ we observe anisotropic peak broadening (see Figure 2 and Figure S2 of the Supporting Information file). Thus, the dehydration reaction involves a change in the microstructure of the material with the appearance of severe microstrains due to the departure of the water molecule from the structure of $CaTeO_3(H_2O)$. The same phenomena is observed after the dehydration of the related compound $SrTeO_3(H_2O)$ in ε-$SrTeO_3$.[10] The layer structure of δ-$CaTeO_3$ (Figure 3b) is built of [CaO_6], [CaO_{6+1}] and [$Te^{IV}O_3E$] polyhedra. For the distorted octahedron related to the Ca1 atom, the Ca–O distances range from 2.20(3) to 2.52(3) Å. For the Ca2 the coordination environment looks like a monocapped and distorted [CaO_{6+1}] octahedron, with six short Ca–O distances, ranging from 2.18(3) to 2.49(3) Å, and one longer d(Ca2–O3) = 2.87(2) Å. The average Ca–O distance related to Ca1 of 2.36 Å is smaller than the one of Ca2 of 2.43 Å. These average distances are also in agreement with those observed in $CaTeO_3(H_2O)$. The trigonal pyramids [TeO_3E] are also more distorted than those observed in $CaTeO_3(H_2O)$. For the Te1 atom the [$Te^{IV}O_3E$] polyhedron is built of two short distances d(Te1–O2) and d(Te1–O3) of 1.84(2) Å and a longer one d(Te1–O1) = 1.99(2) Å. The average distance d(Te1–O) is 1.89 Å with a standard deviation of 0.09 Å. In contrast, the [$Te^{IV}O_3E$] polyhedron related to the Te2 atom is built of one short distance d(Te2–O4) = 1.88(3) Å and two longer ones d(Te2–O5) and d(Te2–O6) of 2.04(3) Å each. The average distance d(Te2–O) is then much larger than those observed for Te1 with d(Te2–O) = 1.99 Å and a standard deviation of 0.09 Å. As previously mentioned, the δ-$CaTeO_3$ structure can also be described as a layer structure. The [CaO_{6+1}] polyhedra are linked together by sharing two trigonal faces and one edge to form infinite layers, parallel to the (*bc*) plane (Figure 4b). The isolated [$Te^{IV}O_3E$] units are attached on both side of the $[CaO_{(6+1)/2}]_\infty$ framework, the Te atoms filling the empty cavities let by the Ca atoms. This new polymorphic δ-$CaTeO_3$ phase keeps the characteristic layers of the hydrated phase $CaTeO_3(H_2O)$. Comparing these two structures along the *b*-axis (Figure 3a), we can see that the layers are stacked along the *a*-axis with the same A-B-A-B sequence. From a first A-layer located at $x \approx 0$, a second B-layer located at $x \approx 1/2$ is generated by the 2_1 helical axis along the

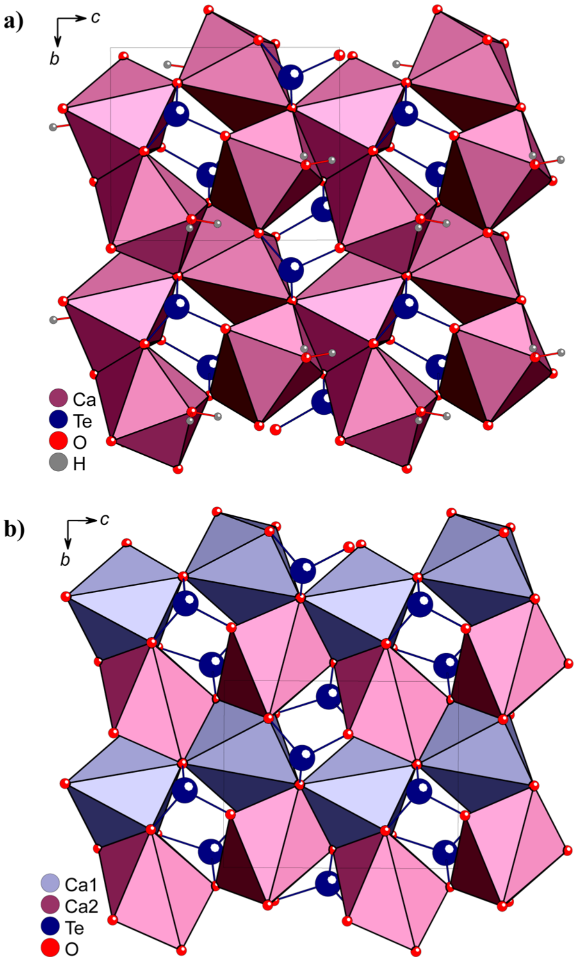

Figure 4. View along the *a*-axis of the infinite layers: (a) in $CaTeO_3(H_2O)$ built from $[CaO_6(H_2O)]$ polyhedra and (b) in δ-$CaTeO_3$ built from $[CaO_6]$ (in blue-gray color) and $[CaO_{6+1}]$ (in plum color) polyhedra.

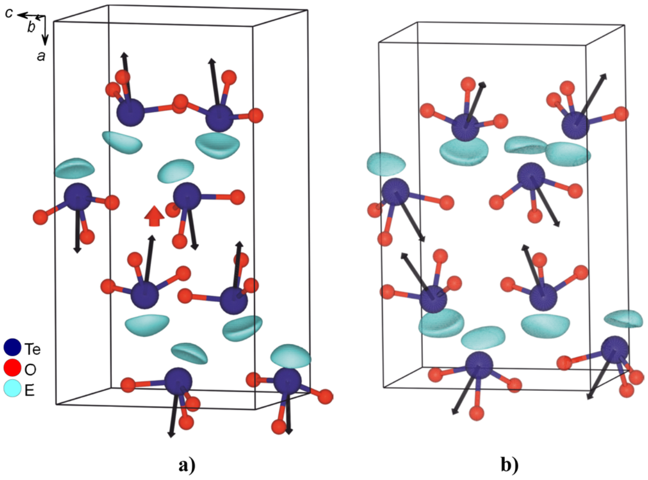

a) b)

Figure 5. Disposition of the $[TeO_3E]$ polyhedra in (a) $CaTeO_3(H_2O)$ and in (b) δ-$CaTeO_3$. The black arrows indicate the direction and the length of the local dipole moment of each polyhedron. The red arrow indicates the direction and the length of the net dipole moment for $CaTeO_3(H_2O)$. The net dipole moment of δ-$CaTeO_3$ is not plotted since its value is close to zero.

a-axis, then again an A-layer is generated at $x \approx 1$. The departure of the water molecule from $CaTeO_3(H_2O)$ involves the condensation of adjacent layers and leads to a reduction of 1.4 Å of the *a* parameter, from a_{hydrated} = 14.785 44(6) Å to $a_{\text{dehydrated}}$ = 13.3647(6) Å. If we look at both structures of $CaTeO_3(H_2O)$ and δ-$CaTeO_3$ along the *c*-axis, (Figure 3b) we observe a change of the stacking sequence: from A-B-A-B for the hydrated phase, to A-A-A-A for the dehydrated phase. During the dehydration process, the intermediate B-layer located at $x \approx 1/2$ is displaced by $1/2\vec{b}$. This translation induces a space group change: from $P2_1cn$ for $CaTeO_3(H_2O)$ to $P2_1ca$ for δ-$CaTeO_3$. The dehydration process described for $CaTeO_3(H_2O)$ can be qualified as topotactic as observed for the related compound $SrTeO_3(H_2O)$. Nevertheless, for the latter, the departure of the water molecule also involves the condensation of the adjacent layers but without any change of the space group that remains $P2_1/c$. Only the monoclinic distortion increases. In this way, the structure of the dehydrated phase ε-$SrTeO_3$ can be described as a three-dimensional framework, since after dehydration the condensed layers are linked through iono-covalent Sr−O bonds of 2.748 Å. In δ-$CaTeO_3$ the shorter Te−O distances between two adjacent layers are 3.18(2) Å for Te1 and 3.34(3) Å for Te2. These distances are too long to allow iono-covalent interactions between tellurium and oxygen atoms. In fact the lamellar type-structure is maintained through van der Waals interactions, which hold together the adjacent layers. Indeed, the presence of permanent dipole moments located on the $[TeO_3E]$ polyhedra in each layer allows such interactions via the electron lone pairs. Between two adjacent layers, we see effectively that the electron lone pairs of one layer point directly toward the Ca atoms of the adjacent layer. Moreover, the metastable behavior of this phase could be due to these weak interactions that maintain the cohesion of the crystal structure. Within δ-$CaTeO_3$ the Te1−E1 distance is slightly longer than the one observed in $CaTeO_3(H_2O)$. The Te1−E1 is 1.46 Å with a charge of −2.72 e^- and a volume of 19.07 $Å^3$. The Te2−E2 is 1.40 Å with a charge of −2.81 e^- and a volume of 19.18 $Å^3$. Individual BVS were also calculated for δ-$CaTeO_3$ and are shown in Table 4. The BVS values for each type of atom stay similar in both $CaTeO_3(H_2O)$ and δ-$CaTeO_3$ structures. Again, the respective calculated values of 3.13 and 1.54 (v.u.) for the Te2 and O6 atoms are lower than the expected values. Since δ-$CaTeO_3$ also exhibits a non-centrosymmetric structure, the local dipole moments were calculated for the $[Te1O_3E]$ and $[Te2O_3E]$ polyhedra (Table 6). The magnitudes are quite similar for both polyhedra with 11.91 and 11.18 D for $[Te1O_3E]$ and $[Te2O_3E]$, respectively, and are comparable to the ones observed for $CaTeO_3(H_2O)$. In the δ-$CaTeO_3$ structure (Figure 5b) the local dipole moments of both polyhedra are also almost aligned antiparallel. The net magnitude of the crystallographic dipole moment is close to zero with 0.47 D along the *a*-axis. Once again, the antiparallel arrangements of the dipole moments with a net dipole moment magnitude close to zero for δ-$CaTeO_3$ might prefigure an even weaker SHG response than the one of $CaTeO_3(H_2O)$.

3.2. Infrared Spectroscopy of $CaTeO_3(H_2O)$.

The Fourier transform infrared (FTIR) spectrum of $CaTeO_3(H_2O)$ (Figure 6) shows bands corresponding to the vibrations of water molecules and $[TeO_3^{2-}]$ oxoanions. On the FTIR spectrum, the trigonal-pyramidal $[TeO_3^{2-}]$ anions show three different groups of bands, as observed for $SrTeO_3(H_2O)$, which own the same type of anion.[10] The proposed band assignments

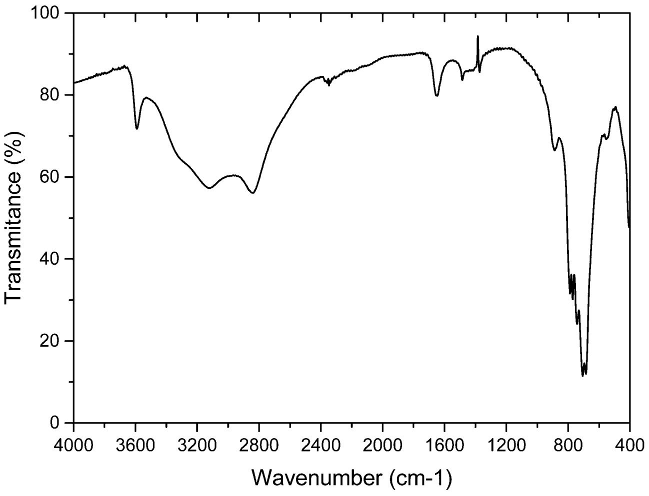

Figure 6. FTIR spectrum of $CaTeO_3(H_2O)$.

are shown in Table 7. The symmetric stretching vibrations $\nu_s(TeO_3)$ correspond to the band around 880 cm^{-1}. The antisymmetric stretching vibrations $\nu_{as}(TeO_3)$ generate split bands with a strong one centered at 698 cm^{-1} and shoulders at 740 and 770 cm^{-1}. This splitting should be due to the low symmetry of the $[TeO_3]$ polyhedra. The band at 545 cm^{-1} corresponds to the symmetric bending vibrations $\delta_{as}(TeO_3)$. The band observed at 1641 cm^{-1} corresponds to the bending vibrations of the water molecules $\delta(H_2O)$. The stretching vibrations $\nu(H_2O)$ generate very broad bands centered around 2830 and 3130 cm^{-1} with a relatively broad and undefined shoulder around 3330 cm^{-1}. The positions of these bands confirm the presence of strong and moderate hydrogen bonds[28] in agreement with the corresponding dD−A distances between oxygen atoms, ranging between 2.70 and 2.86 Å. (Table 5) The last band observed at 3590 cm^{-1} also corresponds to stretching vibrations $\nu(H_2O)$. Nevertheless this band is narrower than the previous ones and may be assigned to the terminal Ow2−H2a bond (Table 5), which is not associated with any hydrogen bond.

Table 7. Assignment of the Bands in the FTIR Spectrum of $CaTeO_3(H_2O)$

assignment	wavenumber (cm^{-1})
$\nu(-OH)$ H_2O	3590 (m); 3330 (sh, m); 3130 (br, s); 2830 (br, s)
$\delta(-OH)$ H_2O	1641 (w)
$\nu_s(TeO_3)$	882 (m)
$\nu_{as}(TeO_3)$	770−740 (sh, s); 698 (vs)
$\delta_s(TeO_3)$	545 (w)
$\delta_{as}(TeO_3)$	411 (w)
ν: stretching; δ: deformation; s: symmetric; as asymmetric	vs: very strong; s: strong; m: medium; w: weak; br: broad; sh: shoulder

3.3. Nonlinear Optical Properties. Since δ-$CaTeO_3$ is metastable, it is very difficult to stabilize it at room temperature. The quenching of a polycrystalline sample of δ-$CaTeO_3$ from 400 °C to room temperature leads to a mixture of the δ- and α-polymorphs. To characterize the nonlinear optical properties of both compounds $CaTeO_3(H_2O)$ and δ-$CaTeO_3$, we decided to perform TR-SHG experiments, from a polycrystalline sample of $CaTeO_3(H_2O)$ (Figure 7). First of all, as expected from the dipole moments calculations, $CaTeO_3(H_2O)$ exhibits a small TR-SHG response of 0.39 × α-quartz. The decrease of the TR-SHG response close to 100 °C corresponds to the beginning of the dehydration process. A plateau is observed between 180 and 280 °C before a last decrease until 390 °C. Granulometric analysis of the as-synthesized polycrystalline sample shows a distribution size ranging between 2 and 400 μm. Nevertheless most of the crystallite sizes range between 6 and 20 μm with a median size close to 14 μm. TR-SHG measurements done on sieved sample, with crystallite sizes inferior to 50 μm (Figure 7), show that the plateau previously observed between 180 and 280 °C has almost gone. Thus, we may conclude that this plateau was due to the presence of crystallite of large sizes in the sample, which could also explain the break observed on the TGA curve. Indeed, the bigger crystallites take longer time to dehydrate than the other ones. After complete dehydration, the SHG response of δ-$CaTeO_3$ falls to 0.06 × quartz. This weaker SHG response compared to that of $CaTeO_3(H_2O)$ was expected, following the dipole moment calculations. Nevertheless this large difference may also be due to the evolution of the crystal quality during the dehydration process. As we see previously, the water escape from the structure of $CaTeO_3(H_2O)$ involves severe microstrains. The decrease of the TR-SHG response during dehydration may then be explained by these strains imposed to the crystallites and also by the scattering of the SHG radiation in the polycrystalline sample.[25,29,30] Note that samples exhibiting crystalline domains were reported to exhibit an increased SHG response (random quasi-phase matching), but this phenomenon is mostly observed for highly transparent cubic samples.[31]

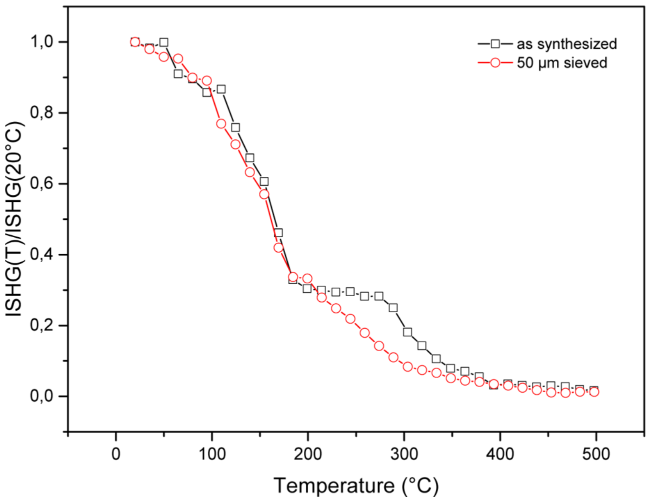

Figure 7. TR-SHG relative intensity response, starting on $CaTeO_3(H_2O)$ polycrystalline samples, as synthesized (□) and 50 μm sieved (○).

3.4. Thermal Behavior. Coupled TG/DSC curves and TD-PXRD diagrams shown in Figure 8a,b were recorded on a polycrystalline sample of $CaTeO_3(H_2O)$. The different reactions are numbered between 1 and 5 and put into brackets in Figure 8a.

The DSC curve shows two peaks corresponding to endothermic reactions: a sharp and very intense one with T_{onset} = 151 °C (reaction 1a) and a diffuse and much less intense with T_{onset} = 205 °C (reaction 1b). These two peaks correspond to the dehydration process of the compound that happens in two steps. On the TG curve, the mass loss of 7.2% represents 0.93 molecule of water per motif $CaTeO_3$. The curve

DOI: 10.1021/acs.inorgchem.5b00037
Inorg. Chem. 2015, 54, 5660−5670

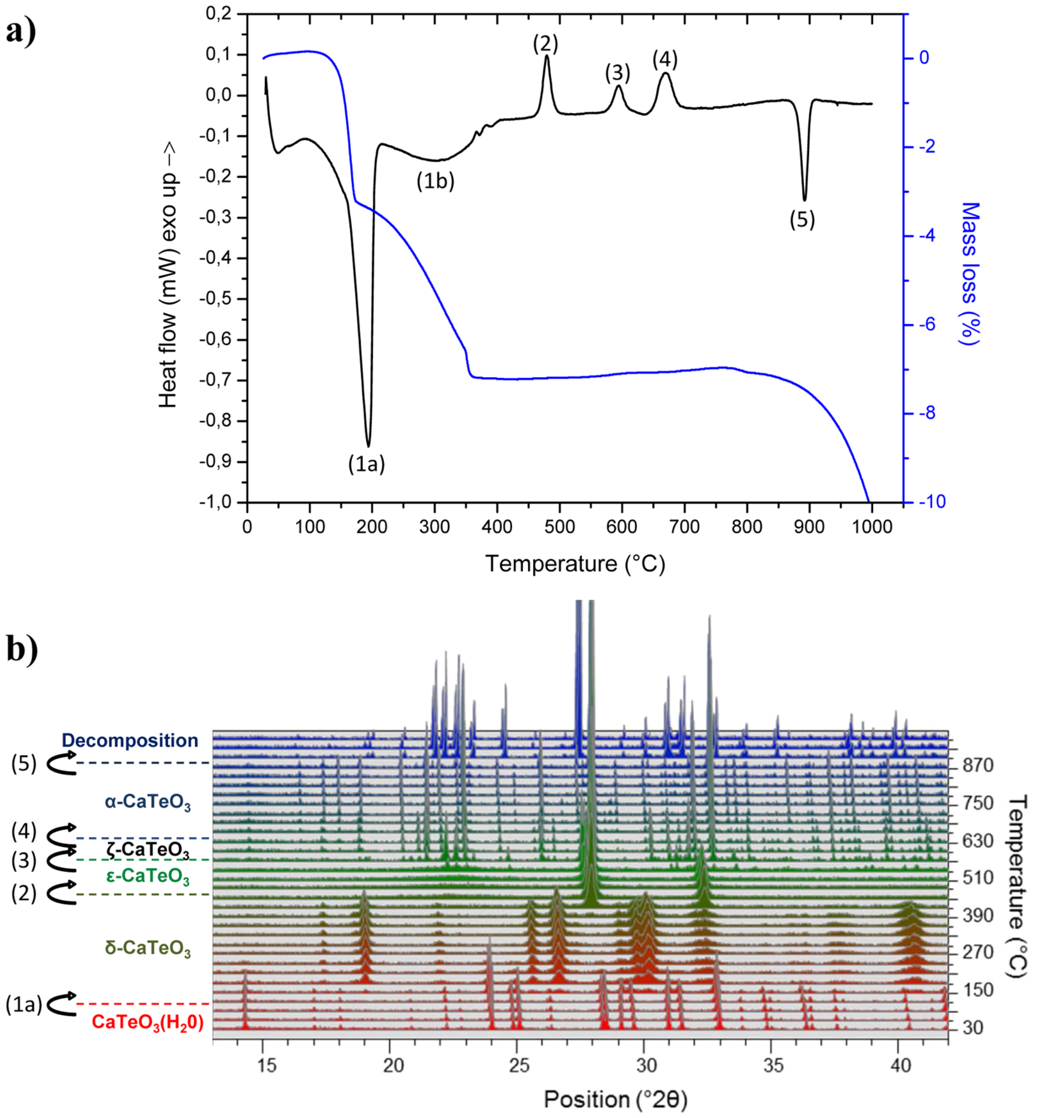

Figure 8. (a) TG (blue) and DSC (black) curves and (b) TD-PXRD diagrams, recorded on powder sample of $CaTeO_3(H_2O)$.

also shows two jumps between 100 and 360 °C corresponding to the two first peaks on the DSC curve. These features may indicate the formation of a hemihydrated phase $CaTeO_3(H_2O)_{0.5}$. Nevertheless, a similar profile is observed on the TR-SHG curve between 30 and 400 °C (Figure 7) for the as-synthesized sample of $CaTeO_3(H_2O)$. Thus, the two steps observed during the dehydration process by TG/DSC may be due to a large distribution of the crystallite sizes and the presence of aggregates. Between 360 and 850 °C no significant mass change is observed. This means that the three exothermic reactions shown on the DSC curve, at T_{onset} of 464 °C (reaction 2), 575 °C (reaction 3), and 648 °C (reaction 4), should correspond to the stabilization process of the $CaTeO_3$ phase, which occurs through successive polymorphic transitions. The last endothermic reaction starts at 883 °C and corresponds to the decomposition of $CaTeO_3$.

These transitions were also observed by TD-PXRD measurements. The onset temperatures of each reaction found on the DSC curve are reported as dotted lines in Figure 8b. The light shifts between the transition temperatures determined from DSC, and TD-PXRD measurements can be explained by the difference of increasing temperature rates used in both experiments. All PXRD patterns between 30 and 120 °C correspond to the well-crystallized hydrated phase $CaTeO_3(H_2O)$. Above 120 °C $CaTeO_3(H_2O)$ is dehydrated into ε-$CaTeO_3$ (reaction 1a). This dehydration reaction occurs until 270 °C. The PXRD diagrams between 150 and 270 °C do not evidence a novel hemihydrated phase: $CaTeO_3(H_2O)_{0.5}$. Indeed, all reflections of these diagrams can be indexed with both phases $CaTeO_3(H_2O)$ and ε-$CaTeO_3$. It confirms that the two steps of the dehydration reaction observed on the TG/DSC curves are due to a large distribution of the crystallite sizes and the presence of aggregates. This also agrees with the temperature shifts observed between the X-ray diffraction experiment and thermal analysis.

At 300 °C the diffraction peaks of the dehydrated phase $CaTeO_3(H_2O)$ have completely disappeared, and the new phase δ-$CaTeO_3$ that only exists between 300 and 420 °C is metastable. Above 420 °C, we observe a new transition (reaction 2). The PXRD diagram obtained after this transition at 450 °C does not correspond to any known phases listed in the Ca−Te−O phase diagram. This new metastable phase may be another original polymorphic phase ε-$CaTeO_3$. On the PXRD diagram at 570 °C several extra peaks appear. This is the beginning of the reaction 3, related to the transformation of ε-$CaTeO_3$ into a sixth polymorph ζ-$CaTeO_3$. Since the PXRD diagrams between 600 and 660 °C do not correspond to any known phases, ζ-$CaTeO_3$ is a novel polymorphic phase. Until now, no unit cell was found for ζ-$CaTeO_3$. Nevertheless, these diagrams can be partially indexed with the tetragonal unit cell of the known α-$CaTeO_3$ phase.[7] Thus, the structure of this novel polymorph ζ-$CaTeO_3$ should be related to the α-$CaTeO_3$ structure. Indeed, all the PXRD diagrams above 690 °C refer to the known polymorph α-$CaTeO_3$. So the reaction 4 is related to the transformation of ζ-$CaTeO_3$ into α-$CaTeO_3$. Finally, above 883 °C (reaction 5) α-$CaTeO_3$ starts to decompose into Ca_3TeO_6[32] with a simultaneous evaporation of TeO_2, agreeing with the mass loss shown on the TGA curve.

4. CONCLUDING REMARKS

Following the previous study of $SrTeO_3(H_2O)$ and ε-$SrTeO_3$, this work confirms the potential of hydrothermal synthesis of hydrated oxotellurate (IV) $MTeO_3(H_2O)$ (M = Ca, Sr) combined with dehydration reaction to generate new $MTeO_3$ polymorphs. Moreover, we have shown that this method allows the preparation of non-centrosymmetric compounds $CaTeO_3(H_2O)$ and δ-$CaTeO_3$. First investigations of thermal analysis and TD-PXRD also show three successive polymorphic transformations between 420 and 880 °C. Above 420 °C the δ-$CaTeO_3$ polymorph starts to transform to a novel metastable ε-$CaTeO_3$ polymorph, which transforms into ζ-$CaTeO_3$, above 570 °C. Finally the last polymorphic transformation occurs above 690 °C and leads to the formation of the known α-CaTeO3 polymorph. These polymorphic transformations are all endothermic and may correspond to successive stabilization reactions that lead to the stable and well-crystallized polymorphic phase α-$CaTeO_3$. This hypothesis should be confirmed by structural characterizations of the intermediate polymorphic phases, namely, ε-$CaTeO_3$ and ζ-$CaTeO_3$, which should be shortly achieved and published.

5. ACKNOWLEDGMENTS

This work was done with the support of the French national computer center IDRIS under Project No. 081842 and the regional computer center CRIHAN under Project No. 2007013.

The authors thank S. Colin and J. Lecourt for the TG/DSC analyses. We also thank B. Raveau for his support and scientific exchanges.

■ ASSOCIATED CONTENT

Ⓢ Supporting Information

Crystallographic information files (cif-files) for $CaTeO_3(H_2O)$ and δ-$CaTeO_3$, SEM images of $CaTeO_3(H_2O)$ crystallites, energy-dispersive X-ray spectroscopy analyses of $CaTeO_3(H_2O)$ crystallites, comparison of the diffraction peak widths between $CaTeO_3(H_2O)$ and δ-$CaTeO_3$, SHG net intensities versus wavelength for $CaTeO_3(H_2O)$ and δ-$CaTeO_3$ at room temperature, granulometric analysis of "as synthesized" and sieved $CaTeO_3(H_2O)$ powder sample. The Supporting Information is available free of charge on the ACS Publications website at DOI: 10.1021/acs.inorgchem.5b00037. Additional crystallographic information on each structure can be obtained from the Fachinformationszentrum Karlsruhe, D-76344 Eggen-steinLeopoldshafen, Germany (e-mail: crysdata@fiz-karlsruhe.de or http://www.fiz-karlsruhe.de/request_for_deposited_data.html) on quoting the CSD Deposition Nos. 428797 for $CaTeO_3(H_2O)$ and 428798 for δ-$CaTeO_3$.

■ AUTHOR INFORMATION

Corresponding Author

*E-mail: nicolas.barrier@ensicaen.fr.

Notes

The authors declare no competing financial interest.

■ REFERENCES

(1) Hahn, T. *International Tables for Crystallography;* D. Reidel Publishing Compagny: Dordecht, The Netherlands, 1983.

(2) Halasyamani, P. S.; Poeppelmeier, K. R. *Chem. Mater.* **1998**, *10*, 2753−2769.

(3) Bergman, J. G.; Boyd, G. D.; Ashkin, A. *J. Appl. Phys.* **1969**, *40*, 2860−2863.

(4) (a) Yamada, T.; Iwasaki, H. *J. Appl. Phys.* **1973**, *44*, 3934−3939. (b) Simon, A.; Von der Mühl, R.; Ravez, J.; Hagenmuller, P.; Pascual, J.-F. *Mater. Res. Bull.* **1979**, *14*, 27−32. (c) Dityat'ev, O. A.; Yu. Stefanovich, S.; Prituzhalov, V. A.; Dolgikh, V. A. *Inorg. Mater.* **2004**, *40* (7), 740−743.

(5) Rai, R.; Sharma, S.; Choudhary, R. N. P. *J. Mater. Sci. Lett.* **2002**, *21*, 297−299.

(6) (a) Yamada, T.; Iwasaki, H. *Appl. Phys. Lett.* **1972**, *21*, 89−90. (b) Yamada, T. *Rev. Electr. Comm. Lab.* **1975**, *23*, 564−568. (c) Dityatiev, O. A.; Berdonosov, P. S.; Dolgikh, V. A.; Aldous, D. W.; Lightfoot, P. *Solid State Sci.* **2006**, *8*, 830−835.

(7) Stöger, B.; Weil, M.; Zobetz, E.; Giester, G. *Acta Crystallogr.* **2009**, *B65*, 167−181.

(8) (a) Dityat'yev, O. A.; Berdonosov, P. S.; Dolgikh, V. A.; Aldous, D. W.; Lightfoot, P. *Solid State Sci.* **2006**, *8*, 830−835. (b) Zavodnik, V. E.; Ivanov, S. A.; Stash, A. I. *Acta Crystallogr.* **2007**, *E63*, i75−i76. (c) Zavodnik, V. E.; Ivanov, S. A.; Stash, A. I. *Acta Crystallogr.* **2007**, *E63*, i111−i112. (d) Zavodnik, V. E.; Ivanov, S. A.; Stash, A. I. *Acta Crystallogr.* **2007**, *E63*, i151. (e) Zavodnik, V. E.; Ivanov, S. A.; Stash, A. I. *Acta Crystallogr.* **2008**, *E64*, i52.

(9) (a) Ivankova, E. A.; Samplavskaya, K. K.; Karapet'yants, M. Kh.; Malyutin, S. A.; Mendeleev, D. I. *Izv. Akad. Nauk SSSR, Neorg. Mater.* **1966**, *2*, 896−898. (b) Ivankova, E. A.; Samplavskaya, K. K.; Karapet'yants, M. Kh. *Izv. Akad. Nauk SSSR, Neorg. Mater.* **1967**, *3*, 1712−1714.

(10) Stoeger, B.; Weil, M.; Baran, E. J.; GonzalezBaro, A. C.; Malo, S.; Rueff, J. M.; Petit, S.; Lepetit, M. B.; Raveau, B.; Barrier, N. *Dalton Trans.* **2011**, *40*, 5538.

(11) Brown, I. D. *J. Appl. Crystallogr.* **1996**, *29*, 479.

(12) Brese, N. E.; O'Keeffe, M. *Acta Crystallogr.* **1991**, *B47*, 192.

(13) Louer, D.; Boultif, A. *Z. Kristallogr. Suppl.* **2006**, *23*, 225.

(14) Altomare, A.; Caliandor, R.; Camalli, M.; Cuocci, C.; Giacovazzo, C.; Moliterni, A. G. G.; Rizzi, R. *J. Appl. Crystallogr.* **2004**, *37*, 1025.

(15) Petricek, V.; Dusek, M.; Palatinus, L. *Jana2006,* the crystallographic computing system; Institute of Physics: Praha, Czech Republic, 2006.

(16) (a) Dollase, W. A. *J. Appl. Crystallogr.* **1986**, *19*, 267. (b) March, A. *Z. Kristallogr.* **1932**, *81*, 285.

(17) Stephens, P. W. *J. Appl. Crystallogr.* **1999**, *32*, 281.

(18) Spek, A. L. *Acta Crystallogr.* **2009**, *D65*, 148.

(19) Dovesi, R.; Orlando, R.; Erba, A.; Zicovich-Wilson, C. M.; Civalleri, B.; Casassa, S.; Maschio, L.; Ferrabone, M.; De La Pierre, M.; D'Arco, P.; Noel, Y.; Causa, M.; Rerat, M.; Kirtman, B. *Int. J. Quantum Chem.* **2014**, *114*, 1287.

(20) Peterson, K. A.; Figgen, D.; Goll, E.; Stoll, H.; Dolg, M. *J. Chem. Phys.* **2003**, *119*, 11113−11123.

(21) Habas, M. P.; Dovesi, R.; Lichanot, A. *J. Phys. Cond. Matter* **1998**, *10*, 6897−6909.

(22) Piskunov, S.; Heifets, E.; Eglitis, R. I.; Borstel, G. *Comput. Mater. Sci.* **2004**, *29*, 165.

(23) Gatti, C.; Saunders, V. R.; Roetti, C. *J. Chem. Phys.* **1994**, *101*, 10686−10696.
(24) Otero-de-la-Roza, A.; Johnson, E. R.; Luaña, V. *Comput. Phys. Commun.* **2014**, *185*, 1007.
(25) Kurtz, S. K.; Perry, T. T. *J. Appl. Phys.* **1968**, *39* (8), 3798.
(26) Nielsen, B. R.; Hazell, R. G.; Rasmussen, S. E. *Acta Chem. Scand.* **1971**, *25*, 3037.
(27) Shannon, R. D. *Acta Crystallogr.* **1976**, *A32*, 751.
(28) Libowitzky, E. Correlation of O-H Stretching Frequencies and O-H O Hydrogen Bond Lengths in Minerals. In *Hydrogen Bond Research;* Schuster, P., Mikenda, W., Eds.; Springer-Verlag: Vienna, 1999; pp 103−115.
(29) Dougherty, J. P.; Kurtz, S. K. *J. Appl. Crystallogr.* **1976**, *9* (2), 145−158.
(30) Vogt, H. *Appl. Phys.* **1974**, *5*, 85−96.
(31) Skipetrov, S. E. *Nature* **2004**, *432* (7015), 285−286.
(32) Burckhardt, H. G.; Platte, C.; Troemel, M. *Acta Crystallogr.* **1982**, *B38*, 2450.